

# Robotic automation of *in vivo* two photon targeted whole-cell patch clamp electrophysiology

Luca A. Anecchino<sup>1</sup>, Alexander R. Morris<sup>1</sup>, Caroline S. Copeland<sup>1</sup>, Oshioyenoya E. Agabi<sup>1</sup>, Paul Chadderton<sup>1</sup>, and Simon R. Schultz<sup>1,\*</sup>

<sup>1</sup>Department of Bioengineering and Centre for Neurotechnology, Imperial College London, London, SW7 2AZ, United Kingdom

\*Lead contact. Correspondence: s.schultz@imperial.ac.uk

## SUMMARY

Whole-cell patch clamp electrophysiological recording is a powerful technique for studying cellular function. While *in vivo* patch clamp recording has recently benefited from automation, it is normally performed “blind”, meaning that throughput for sampling some genetically or morphologically defined cell types is unacceptably low. One solution to this problem is to use two photon microscopy to target fluorescently labelled neurons. Combining this with robotic automation is difficult, however, as micropipette penetration induces tissue deformation, moving target cells from their initial location. Here we describe a platform for automated two photon targeted patch clamp recording, which solves this problem by making use of a closed loop visual servo algorithm. Our system keeps the target cell in focus while iteratively adjusting the pipette approach trajectory to compensate for tissue motion. We demonstrate platform validation with patch clamp recordings from a variety of cells in the mouse neocortex and cerebellum.

**keywords:** automated neurophysiology, patch clamp, multiphoton microscopy, robotic automation

## HIGHLIGHTS

- Whole-cell recording and two photon microscopy were integrated to create a novel platform for automated, visually targeted neurophysiological recording *in vivo*.
- A closed loop visual servo algorithm compensates for micropipette-induced soft tissue deformations during penetration.
- The platform can detect, analyse and quantify the level of focus for multiple single visible objects in the field of view while optimising the target focus in real-time, and use this to correct the electrode trajectory.
- The platform has been validated by recording from a variety of fluorescently targeted cell types in mouse neocortex and cerebellum.

## IN BRIEF

We describe a platform for automated two photon targeted patch clamp recording and demonstrate its functionality by recording from a variety of fluorescently targeted cell types in mouse neocortex and cerebellum.

## INTRODUCTION

The patch clamp technique is an electrophysiological method that allows the recording of macroscopic whole-cell or microscopic single channel currents in single cells using glass micropipettes filled with an electrolytic solution (Hamill et al., 1981). Whole-cell recording (WCR) provides excellent mechanical stability and current resolution in comparison to other electrophysiological recording paradigms, and is the “gold standard” for high-fidelity analysis of ion channel biophysics and the electrical activity of excitable cells (DeWeese, 2007; Sakmann and Neher, 1995). WCR enables integrative analysis of the molecular, synaptic and electrophysiological properties of neurons *in vitro* (Blanton et al., 1989; Edwards et al., 1989; Stuart et al., 1993) and *in vivo* (Ferster and Jagadeesh, 1992; Pei et al., 1991), including unanesthetized preparations (Covey et al., 1996; Margrie et al., 2002), and can also be used for gene manipulation by the introduction of plasmid DNA into single cells *in vivo* (Rancz et al., 2011).

When combined with two-photon laser scanning microscopy (2PLSM) (Denk et al., 1990), WCR can be optically targeted to specific cellular structures via synthetic dyes, the use of transgenic animals expressing fluorescent proteins in specific cell types (Komai et al., 2006; Margrie et al., 2003), viral vectors designed to drive expression via cell-specific promoters (Dittgen et al., 2004), or “shadowpatching” (Kitamura et al., 2008). By adaptively planning and executing image-guided pipette motion in the intact brain, it is possible to obtain recordings from specific cells, cell classes or cell compartments (e.g. dendrites) based on morphological, genetic or functional signatures. However, the rheological properties of brain tissue make precise visually guided control of pipette motion challenging. The insertion of a pipette into soft tissue causes viscoelastic morphological deformation, inducing movement of the target. Persistent target position monitoring by an autonomous computer vision system can provide closed-loop visual servoing for robotic micropipette control, allowing automation of the targeting, engagement and patch-clamping of a fluorescently labelled cell.

Automatic patch-clamp technologies have been used for some years in cell culture paradigms (Fertig et al., 2002) and recently, considerable levels of automation have been achieved in “blind” whole-cell patch-clamp recording (Kodandaramaiah et al., 2012) and image-guided automatic pipette positioning for manual patch-clamp *in vivo* (Long et al., 2015). However, a robotic platform capable of achieving visually targeted electrophysiological recording *in vivo*, by automatically performing all steps involved in a visually targeted whole-cell patch-clamp experiment, has not until now been demonstrated.

## RESULTS

### Platform and Process Overview

Here we describe a platform capable of performing both robotic “blind” and two-photon guided WCR *in vivo* (Fig.1a). Our platform integrates a commercial two-photon microscope with a patch clamp rig and a custom developed pressure regulator system controlled by a microcontroller running a proportional-integral-derivative (PID) controller algorithm. Custom developed software written in Labview (National Instruments) controls the whole platform and implements the WCR algorithm (Fig.1b). One difference between our platform and earlier automated blind patch systems (Kodandaramaiah et al., 2012) is the use of closed as opposed to open loop control of pipette internal pressure. As well as allowing a continuous range of pressure values to be selected, and ensuring that the system is robust against fluctuations in input pressure, this is particularly useful for implementing more refined strategies for manipulating pipette internal pressure, mimicking the suction manoeuvres of experienced patch clamp operators (for instance the gradual application of suction during seal formation).

The algorithm operates in voltage clamp, and automatically performs the principal steps involved in a manually targeted WCR experiment (Fig.1c). After filling a pipette with intracellular solution augmented with a dye such as Alexa 594 and loading it into the pipette holder, the internal pressure is automatically set to a high positive value (10-50 kPa, i.e. 100-500 mBar) by the pressure regulator. A high internal pressure in this initial phase minimises pipette blockage rate. The pipette is manually positioned 50-100  $\mu\text{m}$  above the exposed pial surface at the centre of the field of view for acquisition. The dye-filled pipette tip and fluorescent cells are visualised using multiphoton imaging. Images are continuously acquired while the computer vision system identifies visible objects (cells) in the field of view. Absence of tip blockage is confirmed by a low impedance read-out and a small amount of fluorescent

dye ejected from the tip when pressure is applied. The user then focuses on a potential target cell and, if not already acquired, selects it on the screen and saves its 3D location. The system calculates the path of the pipette to the target, aligns its position to the entry trajectory, and rapidly drives it to a point 200-300  $\mu\text{m}$  from the target location.

After pipette positioning, the pipette impedance is checked. If the pipette is not clogged, then automatic approach is initiated. The system automatically guides the pipette toward the target cell while continuously adjusting the trajectory to compensate for target movement throughout the approach process. When the tip is in the vicinity of the target cell (within 20  $\mu\text{m}$ ), the internal pressure is reduced to approximately 5-10 kPa. This process ends when the pipette tip reaches the coordinates of the target cell. If the tip is not already in contact with the membrane at the end of the automatic approach, a small manual adjustment ( $<8 \mu\text{m}$  depending on the particular manipulator used) of the pipette position can be applied to compensate for any positioning inaccuracy. When target engagement is confirmed by an increase in pipette impedance, the automatic sealing process is initiated.

In order to facilitate seal formation, the internal pressure is released and a holding voltage (-70 mV) superimposed on the test signal. This results in hyperpolarization (with step or ramp variations) of the pipette and has been shown to help with seal formation (DeWeese, 2007; Margrie et al., 2002). Although sometimes these two manoeuvres are sufficient for a tight seal, in other cases the application of negative differential pressure is necessary, for which we use the closed loop pressure regulator system. A seal is obtained when the pipette resistance exceeds a user defined threshold (1-1.5 G $\Omega$ ). If seal formation is unsuccessful, repeated attempts to record from the same cell are possible after replacing the pipette. Cell membrane rupture and access to the cell interior is attained by automatically applying a series of suction pulses. A sharp and rapid decrease of the pipette impedance at this stage indicates successful break-in, and attainment of a whole-cell configuration (DeWeese, 2007; Kodandaramaiah et al., 2012; Margrie et al., 2002). A successful trial is confirmed (i) electrophysiologically, by verifying properties such as membrane potential, firing pattern and access resistance (Fig. 1d-f), and (ii) optically, by observing the gradual filling of the target cell with fluorescent internal solution (Fig. 1g).

Fine robotic control of pipette position for automatic navigation and target engagement relies on the real-time analysis of the light signature of the fluorescent targets in the intact brain. The insertion of a pipette into soft tissue causes viscoelastic morphological deformation which, in turn, induces target migration away from its initial position. The pattern of motion of objects and features observed results from the relative motion between the scene and the observer (the scope objective). During the target engagement procedure, the current position of the target (i.e., a cell) needs to be continuously reassessed and the approach trajectory of the pipette re-adjusted. In the following sections, we describe how this is achieved.

## Quantitative analysis of two photon images

Real-time image segmentation is the first step in this process. Two-photon images are acquired and streamed in real-time to a dedicated custom software module responsible for the on-line processing of the incoming data frames. Quantitative information including contour, area, centre of mass, bounding rectangle and contrast level of individual visible objects in each frame is calculated. These values are used to track the movement of the fluorescent targets in space and time. Tracking information is then used to adjust the trajectory and dynamics of pipette navigation towards the optical target.

The data frames broadcast by the two-photon microscope system consist of a stream of 16-bit RGB images. On each image in the stream the following operations are performed: channel separation, Otsu thresholding (Otsu, 1979) with background correction, hole filling, erosion filtering, and particle analysis. Image analysis is performed on either a single channel or a combination of red and green channels, after the different layers in the frame have been separated (see Fig. S1a-e for an example). Otsu interclass variance thresholding with background correction operation allows binary segmentation of the image while performing background correction to eliminate non-uniform lighting effects (Gonzalez and Woods, 2002). This operation is used to identify bright regions corresponding to significant cellular structures for morphological analysis (Fig. S1b). Particle analysis performed on the thresholded segments then provides geometrical information that includes the contour, area, bounding rectangle and centre of mass coordinates (Gonzalez and Woods, 2002). Individually labelled segments are used to define pixel masks and probe pixel intensity values in specific regions of the original image (Fig. S1c-d), allowing calculation of the

contrast-focus score (CFS) for each salient object in the image Fig. S1e. The CFS for object  $i$  is calculated as

$$\text{CFS}_i = \frac{\langle I \rangle_{\text{internal},i} - \langle I \rangle_{\text{external},i}}{\langle I \rangle_{\text{internal},i}} \quad (1)$$

where  $\langle \cdot \rangle_x$  is the image average operator, over the pixels belonging to the region bounded by contour  $x$ , with the internal and external boundaries differing due to the erosion filter. This is calculated for each object in all the planes of the original RGB image.

### Tracking and autofocusing in two photon time-lapse image streams *in vivo*

Target migration is detected by analysing the spatiotemporal variation of the target light signature at different focal planes. Precise object localisation and accurate centroid estimation are prerequisite for reliable determination of motion, prevention of false-positives, and reduction of noise-related ambiguities. However, depending on the velocity and acceleration of the optical targets in the visual scene, disruptions in continuity of optic flow may occur. This translates into fluidity degradation of motion appearance (abrupt motion) resulting from insufficient acquisition rate, and poses motion detection difficulties that conventional tracking methods (Deutscher et al., 2000; Isard and Blake, 1998) struggle to handle (Li et al., 2007). Enlarging the search space is computationally difficult, and generally incapable of identifying targets through frames due to loss of image context, increased background clutter or target migration outside the field-of-view. In addition, objects whose depth from the focal plane varies in excess of a few micrometres suddenly become severely defocused, and their light signature no longer clearly detectable. For a fixed focal length, dynamic repositioning the objective is necessary to maintain acceptable visibility of targets migrating along a trajectory not completely enclosed by a single field-of-view.

Focus variation provides a visual indication that an object is migrating axially (away from the focal plane), and at the same time is a sensitive parameter for regulating object visibility during tracking. The superior optical sectioning capability of two-photon excitation is beneficial in increasing axial resolution but translates to small depth of field, which can be problematic for online three-dimensional target tracking. To preserve object correspondence between image frames and circumvent the intrinsic constraints of a small depth of field and low signal to noise ratio, object detection should be achieved before the autofocusing step. The contour and centre of mass of the target object can then be used, respectively, as a region-of-interest for an *ad hoc* autofocus algorithm, and as the initial location of the object in the solution of the inter-frame correspondence problem (Manzo and Garcia-Parajo, 2015). The main goal of inter-frame object correspondence, in this case, is not to reconstruct the object motion track on the basis of noisy measurements, but to detect the exact position of the target object while automatically keeping it in focus during electrode approach. Contrast based autofocus is achieved by “swiping” the focal plane of the objective over the region of interest and detecting the optical plane along the  $z$ -axis that maximizes the CFS. We take the best focal distance as the maximum of a Gaussian function fitted to the focus scores (see Fig. S1f-h).

### Automatic approach to the target

The rate of viscoelastic deformation of the tissue depends on the dynamics of electrode insertion. By limiting the electrode insertion speed, we limit the distance the target moves between frames, keep it in the field of view by autofocusing, and preserve the continuity of motion appearance even at low frame rates. Keeping inter-frame target migration small allows the particle search space to be restricted, and the correspondence problem to be solved locally rather than globally. Active detection of time-dependent object contours prior to tracking improves performance with fluorescence microscopy images, and does not limit the nature or shape of the object of interest (Manzo and Garcia-Parajo, 2015). This method is capable of detecting multiple objects, analysing and quantifying the level of focus for each single visible object in the field of view, and generating viewpoint motions to optimise the target focus in real-time.

We interleave electrode penetration with target position monitoring. Individual insertion steps are typically set to 3-4  $\mu\text{m}$ , in order to prevent the maximum target migration induced by a single step from exceeding half of the diameter of the smallest structures targeted (i.e. half of  $\approx 5 - 8\mu\text{m}$ ). The actual target migration distance in a step depends on the relative distance from the electrode tip and actual rheological property of the tissue (Cheng et al.,

2008) (i.e., cortical layer, species, temperature, age, etc). A typical approach trajectory, together with corresponding system parameters during approach, sealing and break-in, is shown in Fig.2.

Our system is robust to breathing and heart beat induced target motions, as they tend to induce the target to periodically disappear and reappear at the same point in the image. The interleaved step-and-reacquire method of our targeting strategy ensures that an electrode insertion step will not be executed until the centre of mass coordinate of the target are updated and the electrode trajectory re-aligned. However, excessive breathing and heart beat related movements may still be problematic for detection of object position during tracking, due to degradation of motion fluidity and apparent target deformation.

## Performance evaluation

We successfully used the platform to perform targeted whole-cell patch clamp recordings from fluorescently labelled cells in a number of preparations, as shown in the example of Fig. 1d-g, which shows current clamp traces obtained from a gfp-positive neocortical interneuron in a GAD67-gfp transgenic mouse. Further examples of successful recordings from neocortical interneurons are shown in Fig. 3a-i). We were also able to use GAD67-gfp to target cerebellar Purkinje cells and obtain cell-attached voltage clamp recordings (Fig. S2) and whole-cell recordings. The platform is not limited to the use of transgenic animals expressing fluorescent proteins, however: we were able to target selected pyramidal neurons in the primary visual cortex of wild type mice by bulk loading with Oregon Green BAPTA-1 AM (Fig. S3a-c), and were also successful in targeting astrocytes labelled with Sulforhodamine-101 (Fig. S3d-f).

The platform is capable of achieving gigaseal-tight contact between the patch pipette and cellular membrane, leading to WCR in either visually targeted or blind mode (in the latter case relying only on the pipette impedance signal; see Fig. S4). The quality and stability of the recordings obtained (quantified by input resistance, resting membrane potential, spike amplitude and holding duration) is comparable to reports from both human operators (DeWeese, 2007; Margrie et al., 2002) and other robotic systems (Kodandaramaiah et al., 2012) across a range of recording depths (Fig. 4a-d and Fig. S4d). System performance is summarised in Table 1. A number of further performance characteristics can be appreciated. Firstly, success rates in either robotic or manual two photon targeted mode are lower than for robotic but blind recording. This simply relates to the fact that for "blind" recording, any cell is a potential target. Secondly, in addition to recording quality, the system achieves yields and operational speeds comparable to or exceeding human operators or other automated platforms for both whole cell and cell-attached recording (the success rate for cell-attached recording being equivalent to the seal success rate in Table. 1).

## DISCUSSION

We have here reported the first platform for fully robotic two photon targeted WCR. Our technology platform, building on previous work (Kodandaramaiah et al., 2012), reduces the human variability, attentional load and manual involvement of labour-intensive *in vivo* WCR experiments, lowering the entry barrier and leading to greater potential scalability. We have demonstrated a novel algorithm that circumvents the intrinsic constraints of two-photon imaging during tissue micromanipulation. Integration of a two photon microscope with computer-controlled patch clamp electrophysiology, together with the image processing method developed in this study, allows the selection of target cells based on genetic, morphological and spatial information. One of the key technological challenges to solve was persistent monitoring of the target object position by autonomous computer vision, to assess and compensate for tissue movement induced by insertion of the pipette into the brain. Visual information is acquired from a time-lapse planar image stream by dynamically generating focal plane motion through autofocus methods while acquiring frames. The target is automatically kept in focus by an algorithm controlling the position of the objective lens based on the focus level of the target, and its position relative to the middle of the current field of view.

Pipette contrast is normally obtained by filling the pipette with a fluorescent dye such as Alexa. As the system keeps track of pipette location after initial acquisition, this dye can either be the same colour as the target label, or a different colour, although the latter is normally preferred. One constraint upon system performance can be the release of fluorescent dye from the pipette tip, accumulating in the tissue and increasing background fluorescence. This can compromise contrast and impact image quality, making computer vision and pipette re-acquisition difficult,

especially after multiple insertions. An elegant solution to this problem would be to use quantum dot-coated glass pipettes (Andrásfalvy et al., 2014), which provides stronger two-photon contrast at greater depths, as well as eliminating dye ejection during entry.

The hit rate, recording quality, and time required for WCR using our method is comparable to that of a human operator performing manual two photon targeted recording. In our testing, cell-attached recordings were obtained on 47% of attempts, and a successful whole cell recording was achieved on 22% of occasions (ie just under half of the "seals" were converted to whole cell recordings). Several (average 2.3) seals were achieved per animal, and just over one (1.1) whole cell recording was obtained per animal. Yield was only slightly higher for manual targeted recording (4.9 and 1.6 seals and WCRs respectively). As well as fully robotic use, the platform can be used to accelerate manual two photon targeted patching, and indeed hybrid manual/automated use may enable new recording capabilities such as in vivo targeted recording from fine dendritic processes. The platform is naturally extensible to parallel recordings from multiple micromanipulators/pipettes. As well as enabling the scaling up of two photon targeted WCR, our system is likely to open up new application domains, via selective labelling of sub-cellular structures, and is likely to be applicable to more challenging experimental paradigms, such as targeted WCR of neurons in awake, behaving animals.

Combining the robotic two photon targeted WCR system with functional imaging will enable numerous novel applications in neuroscience, extending our ability to study the molecular and cellular mechanisms of single cell and network neuronal computation. Automated targeted electrophysiological interrogation of specific cells has the potential to provide not only readout of the intrinsic excitability but also a direct means to determine the responsiveness of specific subtypes of neurons to different sensory stimuli, with high sampling throughput in comparison to sampling cells with "blind" approaches. Monitoring additional physiological parameters such as transient changes in intracellular calcium concentration or membrane voltage in neuronal populations will help to forge a direct link between system and cellular neuroscience. Another important application for this system might be assessing electrophysiological responses of individual cells transfected (and labelled) by recombinant viruses, plasmid DNA or peptides suspected to modulate physiological functions. The increasing availability of genetically modified animals showing selective labelling in subpopulations of cells opens up numerous potential applications.

Further automation of procedures such as the fabrication (Pak et al., 2011), loading and installation of fresh pipettes could eliminate time-limiting manual steps, enabling a single operator to run multiple experiments at the same time, either in the same or different animals. As well as enabling hitherto impracticable questions to be addressed concerning neural circuit function, this may be of great utility in testing pharmaceutical and gene therapeutic approaches to treating nervous system disorders.

## **AUTHOR CONTRIBUTIONS**

LAA and SRS conceived and planned the system. LAA designed and developed the system, designed and performed the experiments, and analyzed the data. ARM performed the manual recordings. ARM, CSC and PC provided input on system design, validation and testing. LAA and SRS wrote the manuscript.

## **ACKNOWLEDGMENTS**

This work was supported by BBSRC award BB/K001817/1, Scientifica Ltd, European Union FP7 Marie Curie Initial Training Network 289146, and a Royal Society Industry Fellowship to SRS. We thank S Chakraborty, Y Liu and B Pichler for technical advice and assistance. We thank T Margrie and the Sainsbury-Wellcome Centre for Neural Circuits and Behaviour for the generous gift of GAD-67 gfp transgenic mice.

## **Additional information**

The authors declare no competing financial interests.

## References

- Andrásfalvy, B. K., Galiñanes, G. L., Huber, D., Barbic, M., Macklin, J. J., Susumu, K., Delehanty, J. B., Huston, A. L., Makara, J. K., and Medintz, I. L. (2014). Quantum dot–based multiphoton fluorescent pipettes for targeted neuronal electrophysiology. *Nature Methods*, 11(12):1237–1241.
- Blanton, M. G., Lo Turco, J. J., and Kriegstein, A. R. (1989). Whole cell recording from neurons in slices of reptilian and mammalian cerebral cortex. *Journal of Neuroscience Methods*, 30(3):203–210.
- Cheng, S., Clarke, E. C., and Bilston, L. E. (2008). Rheological properties of the tissues of the central nervous system: A review. *Medical Engineering and Physics*, 30(10):1318–1337.
- Covey, E., Kauer, J. A., and Casseday, J. H. (1996). Whole-Cell Patch-Clamp Recording Reveals Subthreshold Sound-Evoked Postsynaptic Currents in the Inferior Colliculus of Awake Bats. *J. Neurosci.*, 16(9):3009–3018.
- Denk, W., Strickler, J., and Webb, W. (1990). Two-photon laser scanning fluorescence microscopy. *Science*, 248(4951):73–76.
- Deutscher, J., Blake, A., and Reid, I. (2000). Articulated body motion capture by annealed particle filtering. In *Proceedings of the 2000 IEEE Conference on Computer Vision and Pattern Recognition (CVPR 2000)*, volume 2, pages 126–133.
- DeWeese, M. (2007). Whole-cell recording in vivo. *Current Protocols in Neuroscience*, 38:6.22:1–15.
- Dittgen, T., Nimmerjahn, A., Komai, S., Licznarski, P., Waters, J., Margrie, T. W., Helmchen, F., Denk, W., Brecht, M., and Osten, P. (2004). Lentivirus-based genetic manipulations of cortical neurons and their optical and electrophysiological monitoring in vivo. *Proceedings of the National Academy of Sciences of the United States of America*, 101(52):18206–11.
- Edwards, F. A., Konnerth, A., Sakmann, B., and Takahashi, T. (1989). A thin slice preparation for patch clamp recordings from neurones of the mammalian central nervous system. *Pflügers Archiv: European Journal of Physiology*, 414(5):600–612.
- Ferster, D. and Jagadeesh, B. (1992). EPSP-IPSP interactions in cat visual cortex studied with in vivo whole-cell patch recording. *J. Neurosci.*, 12(4):1262–74.
- Fertig, N., Blick, R. H., and Behrends, J. C. (2002). Whole cell patch clamp recording performed on a planar glass chip. *Biophysical Journal*, 82(6):3056–62.
- Golshani, P. and Portera-Cailliau, C. (2008). In Vivo 2-Photon Calcium Imaging in Layer 2/3 of Mice. *Journal of Visualized Experiments*, 13:681.
- Gonzalez, R. C. and Woods, R. E. (2002). *Digital Image Processing*. Prentice Hall.
- Hamill, O. P., Marty, A., Neher, E., Sakmann, B., and Sigworth, F. J. (1981). Improved patch-clamp techniques for high-resolution current recording from cells and cell-free membrane patches. *Pflügers Archiv: European Journal of Physiology*, 391(2):85–100.
- Isard, M. and Blake, A. (1998). CONDENSATION — Conditional Density Propagation for Visual Tracking. *International Journal of Computer Vision*, 29(1):5–28.
- Kitamura, K., Judkewitz, B., Kano, M., Denk, W., and Häusser, M. (2008). Targeted patch-clamp recordings and single-cell electroporation of unlabeled neurons in vivo. *Nature Methods*, 5(1):61–7.
- Kodandaramaiah, S. B., Franzesi, G. T., Chow, B. Y., Boyden, E. S., and Forest, C. R. (2012). Automated whole-cell patch-clamp electrophysiology of neurons in vivo. *Nature Methods*, 9(6):585–7.
- Komai, S., Denk, W., Osten, P., Brecht, M., and Margrie, T. W. (2006). Two-photon targeted patching (TPTP) in vivo. *Nature Protocols*, 1(2):647–52.
- Li, Y., Ai, H., Yamashita, T., Lao, S., and Kawade, M. (2007). Tracking in Low Frame Rate Video: A Cascade Particle Filter with Discriminative Observers of Different Lifespans. In *Proceedings of the 2007 IEEE Conference on Computer Vision and Pattern Recognition*, pages 1–8. IEEE.
- Long, B., Li, L., Knoblich, U., Zeng, H., and Peng, H. (2015). 3D Image-Guided Automatic Pipette Positioning for Single Cell Experiments in vivo. *Scientific Reports*, 5:18426.
- Manzo, C. and Garcia-Parajo, M. F. (2015). A review of progress in single particle tracking: from methods to biophysical insights. *Reports on Progress in Physics*, 78(12):124601.

- Margrie, T. W., Brecht, M., and Sakmann, B. (2002). In vivo, low-resistance, whole-cell recordings from neurons in the anaesthetized and awake mammalian brain. *Pflügers Archiv: European Journal of Physiology*, 444(4):491–8.
- Margrie, T. W., Meyer, A. H., Caputi, A., Monyer, H., Hasan, M. T., Schaefer, A. T., Denk, W., and Brecht, M. (2003). Targeted Whole-Cell Recordings in the Mammalian Brain In Vivo. *Neuron*, 39(6):911–918.
- Nimmerjahn, A., Kirchhoff, F., Kerr, J. N., and Helmchen, F. (2004). Sulforhodamine 101 as a specific marker of astroglia in the neocortex in vivo. *Nature Methods*, 1(1):31–37.
- Otsu, N. (1979). A Threshold Selection Method from Gray-Level Histograms. *IEEE Transactions on Systems, Man, and Cybernetics*, 9(1):62–66.
- Pak, N., Dergance, M. J., Emerick, M. T., Gagnon, E. B., and Forest, C. R. (2011). An Instrument for Controlled, Automated Production of Micrometer Scale Fused Silica Pipettes. *Journal of Mechanical Design*, 133(6):061006.
- Pei, X., Volgushev, M., Vidyasagar, T. R., and Creutzfeldt, O. D. (1991). Whole cell recording and conductance measurements in cat visual cortex in-vivo. *Neuroreport*, 2(8):485–8.
- Rancz, E. A., Franks, K. M., Schwarz, M. K., Pichler, B., Schaefer, A. T., and Margrie, T. W. (2011). Transfection via whole-cell recording in vivo: bridging single-cell physiology, genetics and connectomics. *Nature Neuroscience*, 14(4):527–32.
- Sakmann, B. and Neher, E. (1995). *Single-Channel Recording*. Springer.
- Schultz, S. R., Kitamura, K., Post-Uiterweer, A., Krupic, J., and Häusser, M. (2009). Spatial pattern coding of sensory information by climbing fiber-evoked calcium signals in networks of neighboring cerebellar Purkinje cells. *Journal of Neuroscience*, 29(25):8005–15.
- Stosiek, C., Garaschuk, O., Holthoff, K., and Konnerth, A. (2003). In vivo two-photon calcium imaging of neuronal networks. *Proceedings of the National Academy of Sciences of the USA*, 100(12):7319–24.
- Stuart, G. J., Dodt, H. U., and Sakmann, B. (1993). Patch-clamp recordings from the soma and dendrites of neurons in brain slices using infrared video microscopy. *Pflügers Archiv: European journal of physiology*, 423(5-6):511–518.

## Figure and Table Legends

**Figure 1.** Automated two-photon guided whole-cell recording *in vivo*. (a) Schematic of the apparatus, which consists of a conventional commercial two-photon microscope, a mode-locked Ti-Sapphire laser, a patch setup equipped with programmable 3-axis micromanipulator, a signal amplifier, an analog to digital converter board, a computer and custom-made electro-pneumatic actuator for controlling micropipette internal pressure. (b) Block diagram of the two-photon guided robotic procedure. (c) Stages of the visually guided procedure: setup and pipette placement, tip and target coordinates acquisition, pipette positioning, automatic approach, position compensation, target cell engagement, seal formation and break-in followed by whole-cell configuration. (d) Current-clamp traces during current injection (400 ms-long pulses from -100 to +100 pA in 50 pA steps) and (e and f) at rest for a robotically patched gfp-positive neuron in the neocortex of a GAD67-gfp mouse (f is a zoomed in detail of the underscored section of the trace in e). (g) Two-photon image of the patched neuron and the electrode.

**Figure 2.** Pipette approach trajectory and state during a typical robotic two-photon targeted patching process. (a) Automatic navigation of the pipette towards the target cell, with real-time feedback control of trajectory enabled. (b) Time-course of pipette resistance, current, holding potential, internal pressure and depth during the patching procedure (stages colour coded; numeric labels correspond to points on the approach trajectory in (a)).

**Figure 3.** Further examples of robotic two photon targeted whole-cell recording *in vivo*. (a) Current-clamp traces during current injection (400 ms long pulses from -100 to +100 pA in 50 pA steps) and (b) at rest for a patched neocortical interneuron in the V1 cortex of a GAD67-gfp (depth -113  $\mu\text{m}$  from the brain surface; note compressed timescale relative to (a)). (c) Maximum intensity z-projection of a two photon stack image of the patched neuron and the electrode, acquired after the recording. (d) Current-clamp traces during current injection (400 ms long pulses from -100 to +25 pA in 25 pA steps) and (e) at rest for a patched neuron in the V1 cortex of a GAD67-gfp (depth -102  $\mu\text{m}$  from the brain surface). (f) Maximum intensity z-projection of a two photon stack image of the patched neocortical interneuron and the electrode, acquired after the recording. (g) Current-clamp traces during current injection (400 ms long pulses from -100 to +150 pA in 50 pA steps) and (h) at rest for a patched neuron in the V1 cortex of a GAD67-gfp (depth -142  $\mu\text{m}$  from the brain surface). (f) Maximum intensity z-projection of a two photon stack image of the patched neocortical interneuron and the electrode, acquired after the recording.

**Figure 4.** Visually guided robotic patching achieves similar results to manual targeted patching. Comparison of robotic and manual two-photon targeted recordings obtained from neocortical interneurons in the V1 cortex (triangles for robotic, n=15; x for manual, n=14) and from Purkinje cells in the cerebellum (circles for robotic; n=5). Comparisons are shown as a plot of input resistances obtained versus cell depth (c; left) and mean access resistance  $\pm$  s.e.m. for each condition (c; right), resting potential versus cell depth (d; left) and mean resting potential  $\pm$  s.e.m. for each condition (d; right), spike height versus cell depth (e; left) and mean spike height  $\pm$  s.e.m. for each condition (e; right), holding time versus cell depth (f; left) and mean holding time  $\pm$  s.e.m. for each condition (f; right).

**Table 1.** System performance for robotic two photon guided WCR. Summary performance statistics for 90 patching attempts from 18 animals (1 craniotomy per animal) in robotically automated guidance mode, and 78 attempts from 9 animals (1 craniotomy per animal) in manual guidance mode. Animal age ranges were approximately matched ( $92 \pm 39$  versus  $109 \pm 25$  days postnatal, mean  $\pm$  s.d.). For comparison, the performance of our system in robotic, but "blind" (non-visually targeted) is shown at right. Results are provided as mean  $\pm$  s.e.m. *n* indicates the number of samples for the row statistic - number of patching attempts, number of animals, or number of successful recordings. Success rates in all cases exclude losses due to blockage of a pipette after insertion but before initiating cell approaching. Holding duration statistics for blind robotic recordings are not available, as in these experiments, throughput was prioritised.

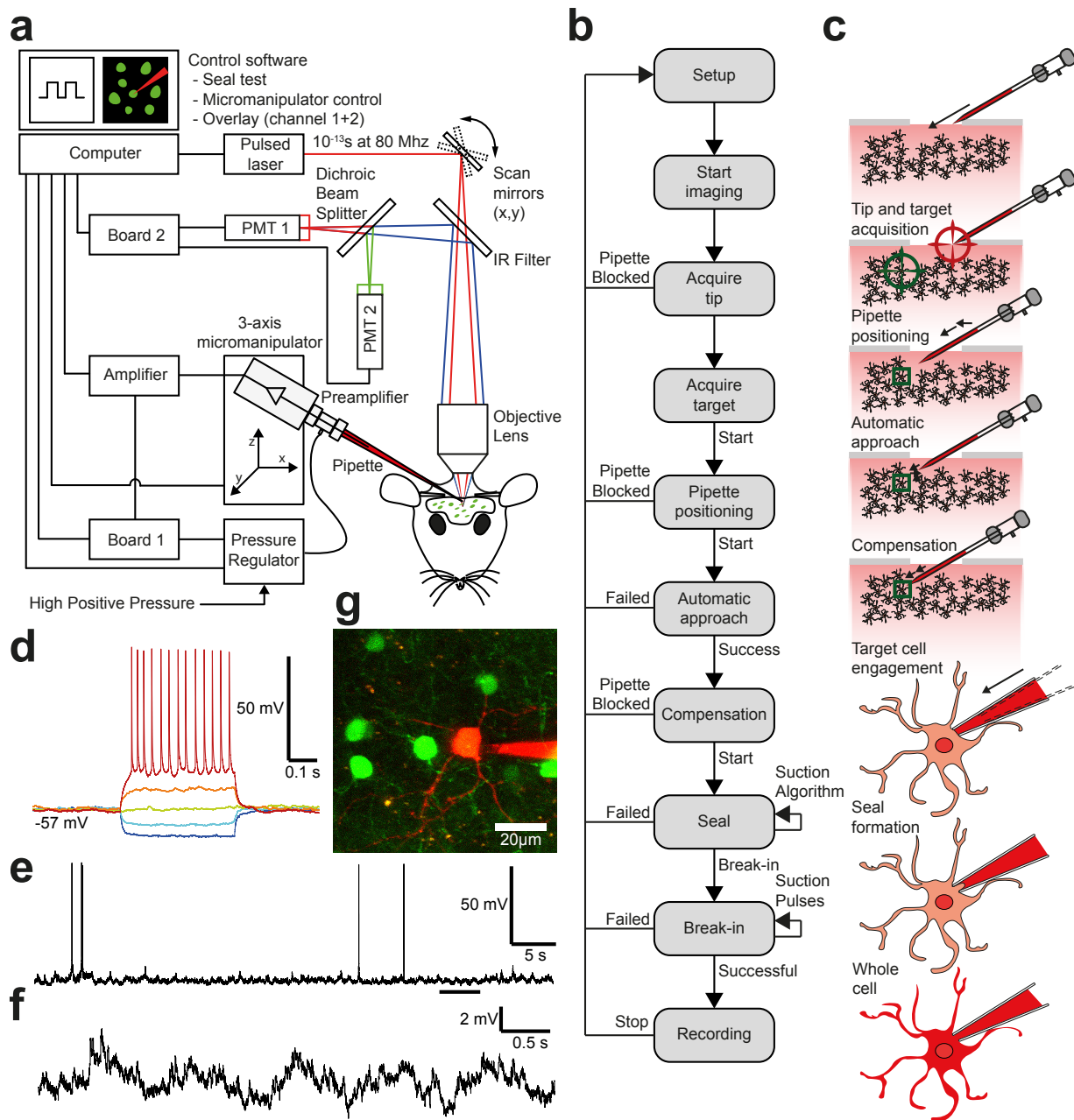
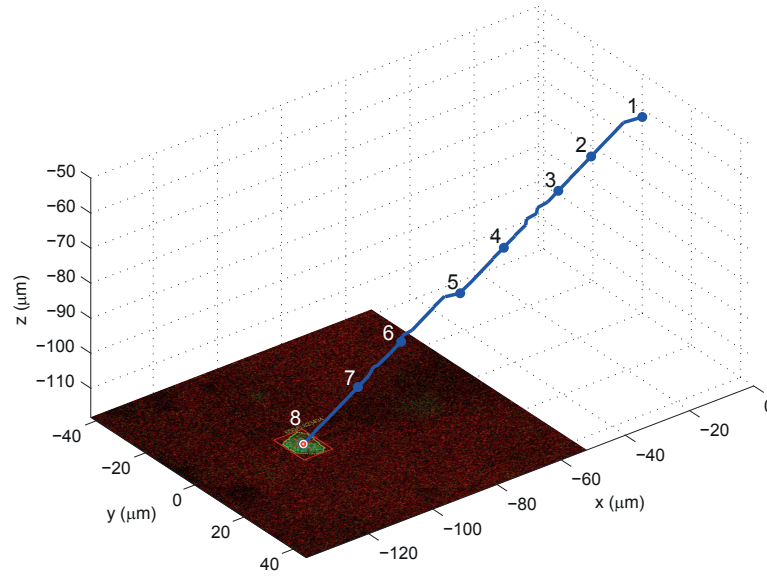
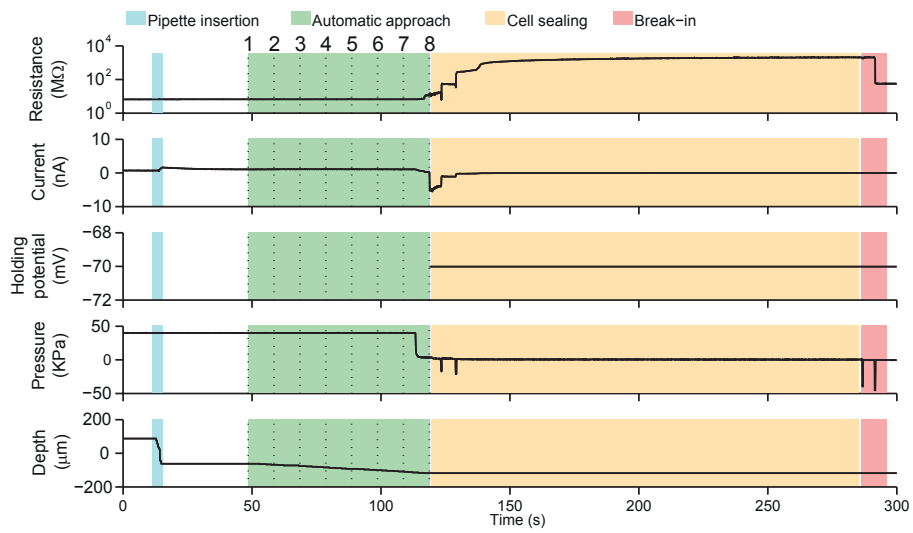
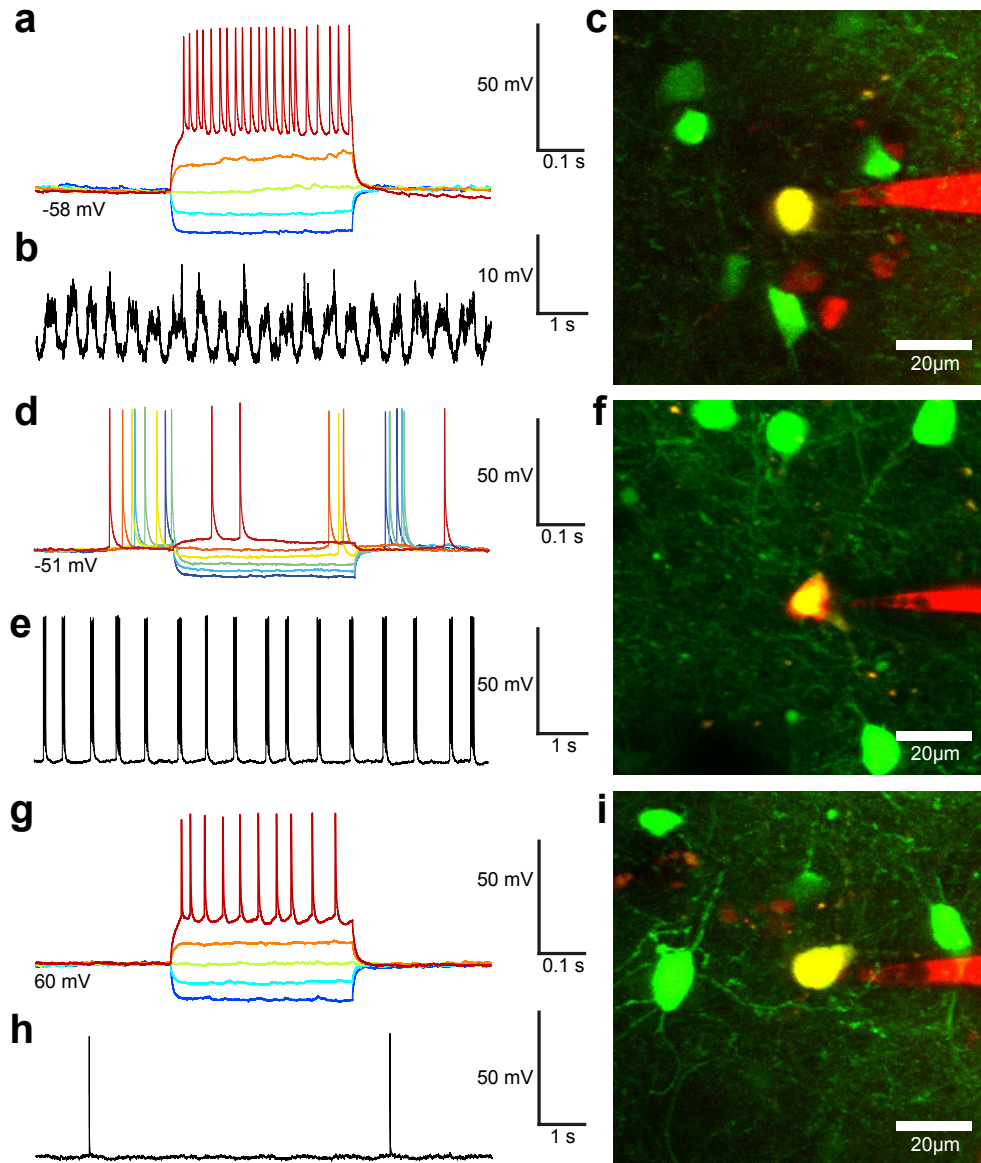
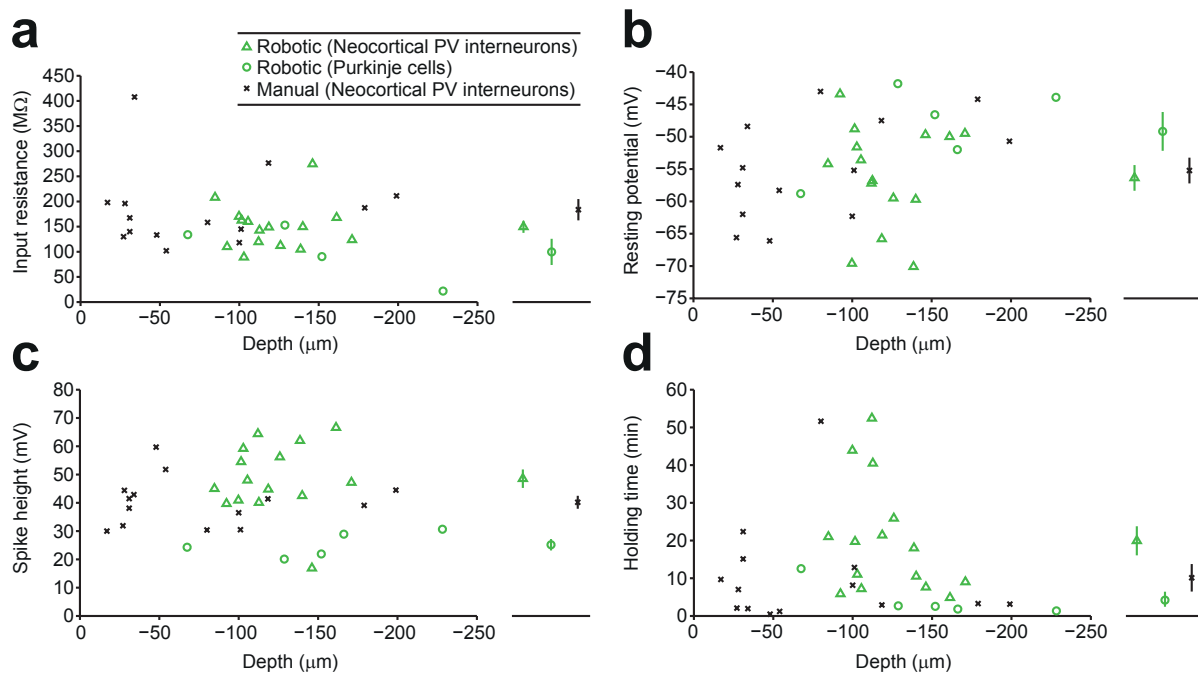


Figure 1

**a****b****Figure 2**



**Figure 3**



**Figure 4**

## Tables

**Table 1.** System performance for robotic two photon guided patch clamp electrophysiology.

	Robotic	<i>n</i>	Manual	<i>n</i>	Blind	<i>n</i>
Seal success rate (%)	46.6	90	56.4	78	74.2	35
WCR success rate (%)	22.2	90	18.0	78	51.4	35
Seals per animal	2.3±0.3	18	4.9±1.0	9	5.2 ± 0.3	5
WCRs per animal	1.1±0.2	18	1.6±0.3	9	3.6 ± 0.4	5
Time to achieve seal (min)	6.0±0.6	20	9.8±1.4	14	3.3 ± 0.4	26
Time to achieve WCR (min)	6.1±0.6	"	10.0±1.4	"	3.6 ± 0.4	18
WCR holding duration (min)	16.6±3.3	"	10.1±3.6	"	-	-
Input resistance (MΩ)	139.2±11.6	"	183.7±21.0	"	64.1 ± 4.2	18
Series resistance (MΩ)	16.0±0.5	"	16.3±0.3	"	14.9±0.5	"
Resting potential (mV)	-54.1±1.8	"	-54.8±2.0	"	-57.8 ± 4.8	"
Spike amplitude (mV)	42.7±10.7	"	40.2±2.3	"	50.1 ± 5.4	"

## STAR METHODS

### CONTACT FOR REAGENT AND RESOURCE SHARING

Further information and requests for resources and reagents should be directed to and will be fulfilled by the Lead Contact, Simon Schultz (s.schultz@imperial.ac.uk)

### EXPERIMENTAL MODEL AND SUBJECT DETAILS

All procedures were carried out in accordance with institutional animal welfare guidelines and licensed by the UK Home Office under Project License 70/9095. Adult male and female mice (c57BL/6 wild type mice, 8–12 weeks old, from Harlan UK, or GAD67-gfp, 2–5 months old), were housed in standard cages in the Imperial College London animal facility with ad libitum food and water in a controlled 12 hours light-dark cycle environment, with standard monitoring by veterinary staff.

### METHOD DETAILS

#### Surgical Procedures

On the day of the experiment, the animals were anesthetized with a mixture of Fentanyl (Sublimase; 0.05 mg/kg), Midazolam (Hypnovel; 5 mg/kg) and Medetomidin (Domitor; 0.5 mg/kg) injected intraperitoneally and redosed at 90-120 min intervals with 50% of the initial dose as needed. Throughout all experiments, a rectal probe and a feedback-controlled heating pad maintained the animal temperature at  $37 \pm 1^\circ\text{C}$ . A craniotomy (diameter  $1.5 \pm 0.5$  mm) was made over visual cortex (1.5 mm anterior to lambda, 3.5 mm lateral from the midline) or over the cerebellum (1.0 mm posterior to lambda, midline) and a durotomy performed with forceps. Artificial cerebrospinal fluid (ACSF, consisting of 126 mM NaCl, 3 mM KCl, 1.25 mM  $\text{NaH}_2\text{PO}_4$ , 2 mM  $\text{CaCl}_2$ , 2 mM  $\text{MgSO}_4$ , 24 mM  $\text{NaHCO}_3$  and 10 mM glucose) was applied to keep the exposed cortex moist until pipette insertion. An incision in the middle upper part of the muscles over the neck was performed to firmly host an Ag/Cl grounded reference electrode (model EP1 Ag/AgCl half-cell electrode 1.0 mm diameter  $\times$  2.5 mm length; WPI).

#### Electrophysiology and Cellular Labelling

Whole-cell recordings were obtained upon establishing an electrical connection between a low-resistance (5 to 7 M $\Omega$ ) micropipette (Sakmann and Neher, 1995) and an excitable cell membrane. We used heat-polished glass pipettes fabricated from filamented borosilicate capillaries (76 mm, 1.5 mm outer diameter, 0.84 mm inner diameter; code 1B150F-3 from WPI) pulled using a vertical pipette puller (model PC10, Narishige) and filled with an electrolytic solution. The internal solution was composed of 135 mM K-methanesulphonate, 7mM KCl, 10 mM HEPES, 2mM Mg-ATP, 2mM  $\text{Na}_2$ -ATP, 0.5 mM  $\text{Na}_2$ -GTP, and 0.05 mM ethylene glycol tetra-acetic acid (EGTA); the PH was 7.28 (measured with an Orion 9156BNWP combination pH electrode; Thermo Scientific); osmotic concentration was equal to 290 mmol/kg (measured with a vapour pressure osmometer model Vapro 5600 by Wescor Biomedical Systems). In some cases, two photon imaging contrast was due to endogenous labelling in GAD67-gfp transgenic mice. In other experiments, wild type mice were fluorescently labelled with OGB-1 AM and SR-101, using previously established techniques (Golshani and Portera-Cailliau, 2008; Nimmerjahn et al., 2004; Schultz et al., 2009; Stosiek et al., 2003).

#### System design

The automated two-photon guided whole-cell recording apparatus is based on the integration of a commercial two-photon microscope (Scientifica Ltd.) controlled by a data acquisition board (DAQ PCI-6110, National Instruments) and other devices used in a conventional *in vivo* electrophysiological setup, such as a 3-axis micromanipulator (Multistar patch clamp manipulator, Scientifica Ltd.), a signal amplifier (Multiclamp 700B, Axon Instruments), a second data acquisition board (DAQ USB-6211, National Instruments) for electrophysiological data acquisition, and a personal computer running Microsoft Windows 7. In addition to this, we incorporated a custom made pressure regulator system controlled by a commercial microcontroller (Arduino Due board based on the Atmel SAM3X8E ARM Cortex-M3 CPU).

Two-photon laser excitation is generated by a commercial mode-locked Ti-sapphire laser (Mai Tai HP) and scanned by two galvanometric scanning mirrors (6215H-671XX Cambridge Technology). Fluorescence signal collection is performed using two photo-multiplier tubes (R3896s, Hamamatsu Photonics), a dichroic beam splitter (T565LPXR, Chroma Technology) and two optical filters (ET620/60M-2P and ET525/50M-2P, Chroma Technology). Sciscan software (Scientifica Ltd) controls beam scanning and signal collection through a data acquisition board. Two-photon images of fluorescently labelled neuronal tissue are reconstructed and streamed, in real-time, to a dedicated custom software module responsible for object identification, target selection (via a point-and-click graphical user interface) and tracking. Tracking information is then used to control the manipulator and adjust the trajectory and dynamics of pipette navigation towards the target.

The manipulator is connected to the computer through a serial COM port and is controlled via a custom written library of functions based on National Instruments VISA drivers (National Instruments). Pipette electrode visualisation in two-photon images is enabled by augmenting the internal solution with a fluorescent dye (e.g. Alexa Fluor 594 hydrazide, Molecular Probes). During the entire patch clamp attempt and until the beginning of recording session, this amplifier generates a square wave seal test signal (10 mV in amplitude at 10 Hz) used to continuously monitor pipette impedance. Seal test response and electrophysiological signals are amplified by a Multiclamp Amplifier (700B, Molecular Devices) and acquired by a second data acquisition board (DAQ USB-6211, National Instruments). The Multiclamp 700B amplifier is controlled through a software module based on a dynamic linking library (dll; by Axon Instruments). The electrode seal test signal is sampled by the DAQ USB-6211 board at 20 KHz and filtered using a low pass digital Bessel filter (10 KHz-cutoff frequency). The resistance is calculated as the ration of the applied voltage and the measured peak-to-peak current at each cycle of the test signal.

The custom made pressure regulator is controlled in closed-loop by a microcontroller running a proportional-integral-derivative controller (PID controller) algorithm. The PID controller regulates the current flowing through the valves of the system. The schematic of the design is reported in Supplementary Figure S5. The input pressure is provided by a fixed pressure reservoir regulated by a wall mounted tap ([E1] - FRLI 1/4, 2000 L/m, Beefittings). Further pressure reduction is performed through two manually regulated flow control studs elbow ([E2, E3] – AS 2211F-01, SMC Pneumatics). E2 and E3 constitute the positive pressure supply to two electrically regulated proportional solenoid valves ([A and B] – PVQ33-5G-16, SMC Pneumatics) regulating the flow in the branch controlling positive and negative pressure in the pipette. The positive branch consists of the pneumatic series E3-A while the negative branch is E2-B-D. Component D is a Venturi vacuum ejector ([D] - ZH10DL-06-06-08, SMC Pneumatics). The positive branch includes another manually regulated flow control stud elbow ([E3] - BSPT-PCSET 06-1/8, Beefittings) serving as an exhaust port. The positive and negative branches are connected respectively to the normally open and normally closed input of a 3 port solenoid valve ([C] - VQ110U-5M-Q, SMC Pneumatics). All the pneumatic components of the system are mounted on a custom designed transparent poly-methyl-methacrylate (Plexiglas) platform. The levels of pressure used during pipette initial insertion or automatic navigation to a target are constant and pre-defined in the configuration of the system. However, the adaptive suction for seal enhancement procedure uses a more refined method which constantly monitor the pipette resistance, and depending on its value and rate of change dynamically alters the pressure SP of the PID controller, and reproduces the suction manoeuvres of human patch clamp operators. Suction is applied if the pipette impedance is failing to increase in excess of another threshold value  $S_{th}$  over a time period  $T_{seal}$  and its value is lower than 15% of the target seal resistance. The algorithm has a time limit to attain a seal or reflect a failure.

## QUANTIFICATION AND STATISTICAL ANALYSIS

Quantitative results describing system performance can to be found in Table 1, with further description in the caption thereof, and in Figure 4, with description in the caption thereof.

## DATA AND SOFTWARE AVAILABILITY

The LabView software component of the platform has been made available at <http://www.github.com/schultzlab/rita>.

## **KEY RESOURCES TABLE**

This table has been provided as a separate file.

## Supplemental Material

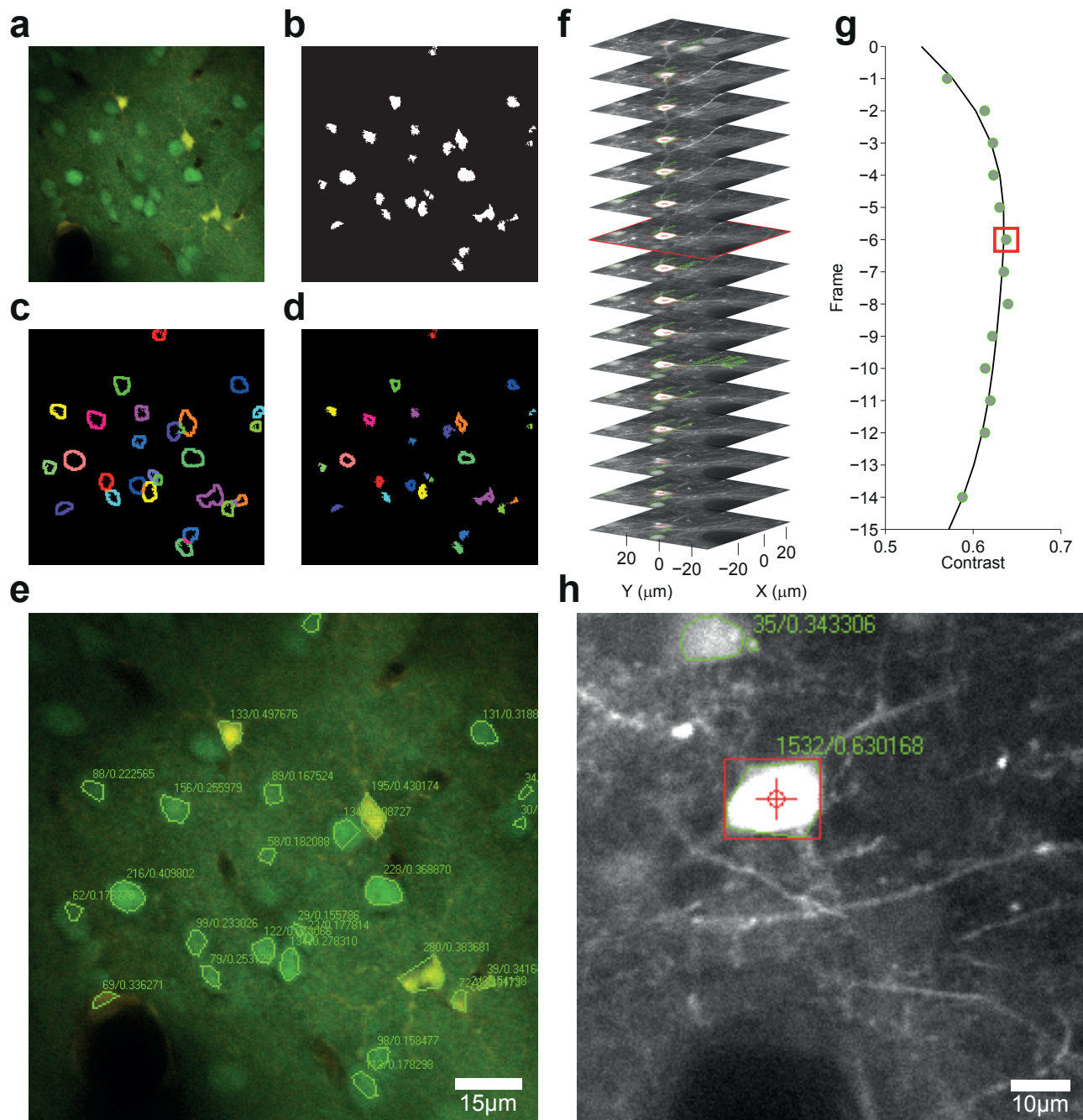


**Figure S1.** Related to Figure 1. Automatic analysis of two-photon images. (a) Initial image, an example of an RGB frame showing cortical tissue loaded with Oregon Green Bapta-1 AM and Sulforhodamine 101. (b) Erosion filtered version of the binary image obtained after thresholding the green channel (c) Set of masks used to select the external (c) and internal (d) boundaries of each segmented cell. (e) Analysis information is overlaid on the original image in real-time. (f) The focal plane is swiped over the evaluation volumetric region containing the target object and the contrast level of its light signature measured for each frame. (g) The plane with the best focus is identified by taking the maximum of a Gaussian function fitting the focus level of each plane. (h) At the end of the autofocus procedure the focal plane is set at the depth for which the maximum contrast was detected.

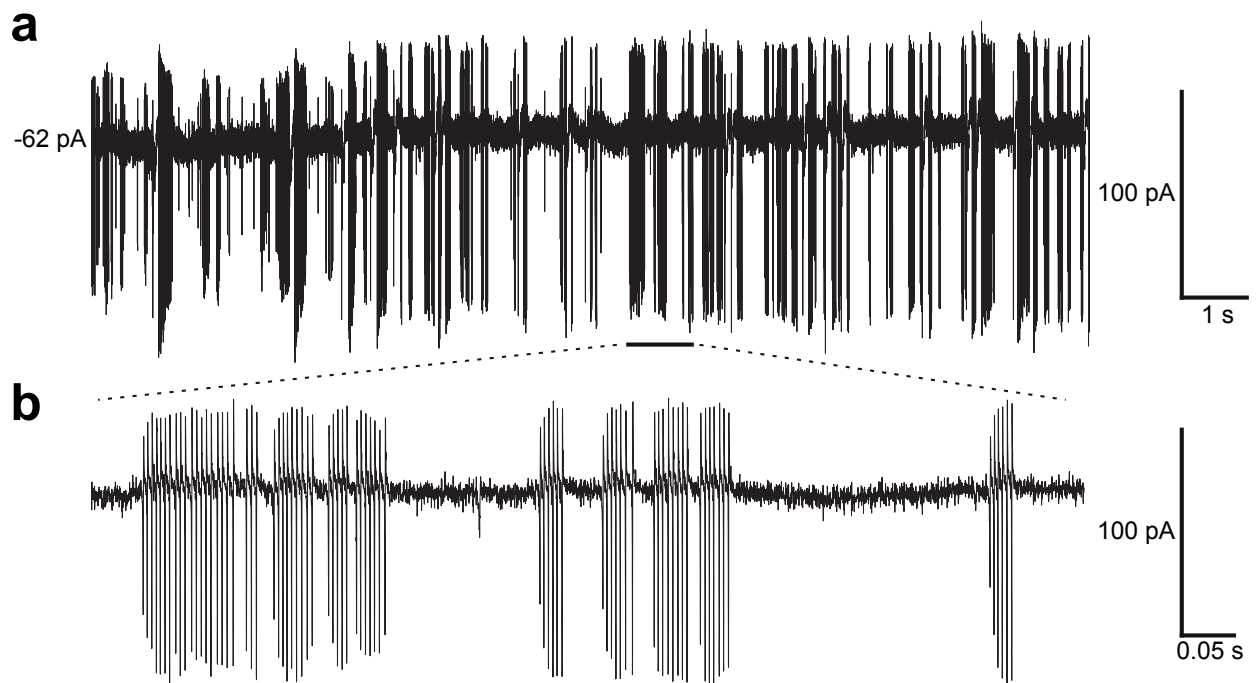


**Figure S2.** Related to Figure 3. Robotic cell-attached recordings. (a) Voltage clamp recording for a cerebellar Purkinje cell in a *GAD67-gfp* mouse, at a depth of  $135\ \mu\text{m}$ . (b) Expanded detail of the underscored section of the trace in (a).

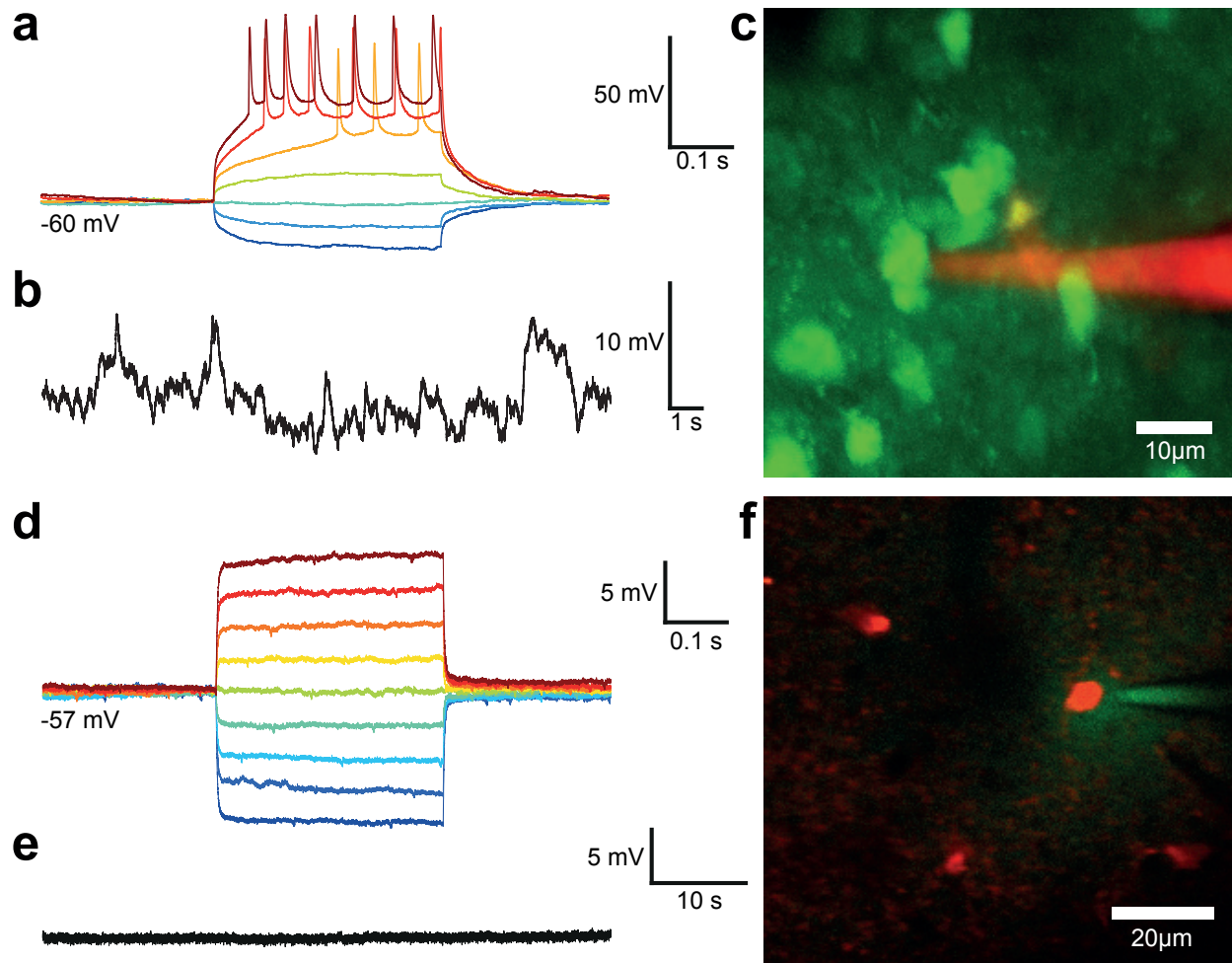


**Figure S3.** Related to Figure 3. (a) Current-clamp traces during current injection (400 ms long pulses from -50 to +100 pA in 25 pA steps) and (b) at rest for a patched neocortical neuron in the V1 cortex of a wild-type mouse bulk loaded with OGB-1 AM (depth -186  $\mu\text{m}$  from the brain surface). (c) Maximum intensity z-projection of a two photon stack image of the patched neuron and the electrode, acquired after the recording. (d) Current-clamp traces during current injection (400 ms long pulses from -100 to +100 pA in 50 pA steps) and (e) at rest for a patched neocortical astrocyte in the V1 cortex of a wild-type mouse bulk loaded with Sulforhodamine 101 (depth -137  $\mu\text{m}$  from the brain surface). (f) Two photon image of the patched astrocyte, acquired at the end of the targeting process.

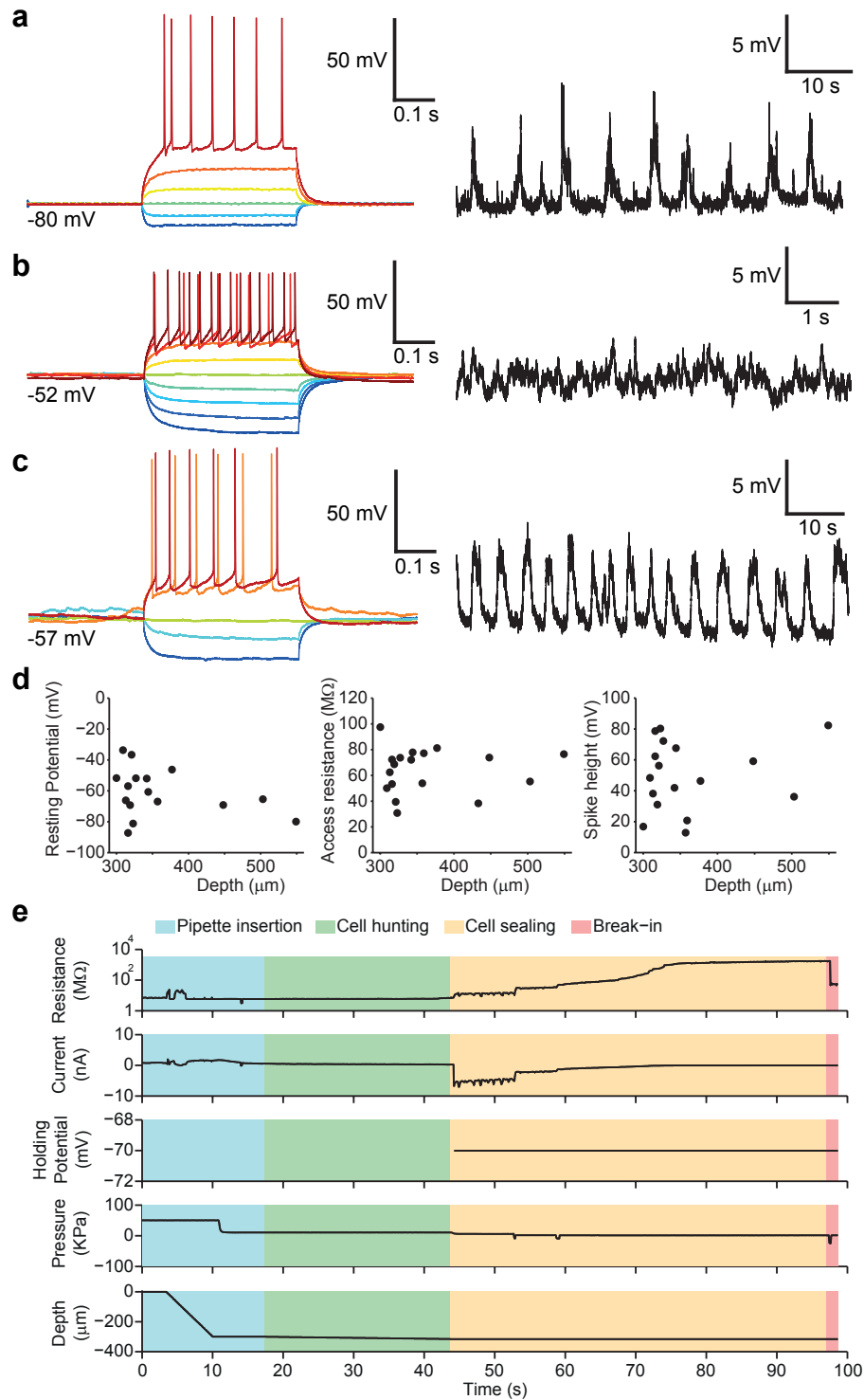


**Figure S4.** Related to Figure 3. Automatic blind whole cell recordings *in vivo*. (a; left) Intrinsic response of a regular spiking (RS) neuron during hyperpolarising and depolarising current injection applied through the recording pipette electrode (400 ms-long current transients from -100 to +150 pA at 50 pA increase in steps); pipette tip depth was -549  $\mu$ m from the pial surface. (a; right) Current clamp trace for the same RS neuron at rest. (b; left) Intrinsic (Caption continued on following page)

response of a fast spiking (FS) neuron during hyperpolarising and depolarising current injection applied through the recording pipette electrode (400 ms-long current transients from -100 to 100 pA at 25 pA increase in steps); pipette tip depth was -342  $\mu\text{m}$  from the pial surface. (b; right) Current clamp trace for the same RS neuron at rest. (c; left) Intrinsic response of a regular spiking (RS) neuron during hyperpolarising and depolarising current injection applied through the recording pipette electrode (400 ms-long current transients from -100 to 100 pA at 50 pA increase in steps); pipette tip depth was -316  $\mu\text{m}$  from the pial surface. (c; right) Current clamp trace for the same RS neuron at rest. (f) Characterization of robotic blind recordings obtained from neurons in the V1 cortex (n=18) shown as a plot of resting potential versus cell depth, input resistances versus cell depth and spike height versus cell depth. (e) Example of time-courses of pipette resistance, current, holding potential, internal pressure and pipette depth. Time intervals relative to the different stages of the automated patching algorithm are colour coded. During the insertion process (in light blue) a relatively high internal pressure (50-100 KPa) was applied and the pipette was rapidly guided to a user defined depth. The pressure was then reduced to a relatively low level (5-10 KPa) and the hunting process (in green) initiated. A 15-20% increase in pipette resistance over three consecutive insertion steps indicates cell detection and initiates the sealing process (in yellow). Positive pressure was released and a holding potential of -70 mV applied to the pipette electrode. Adaptive suction was applied by the system to help attaining a tight seal. Cell break-in (in pink) was attained by applying one or more suction pulses. The cell patched at the end of this automatic patch clamp trials was a regular spiking neuron (intrinsic response shown in Fig.S4c).

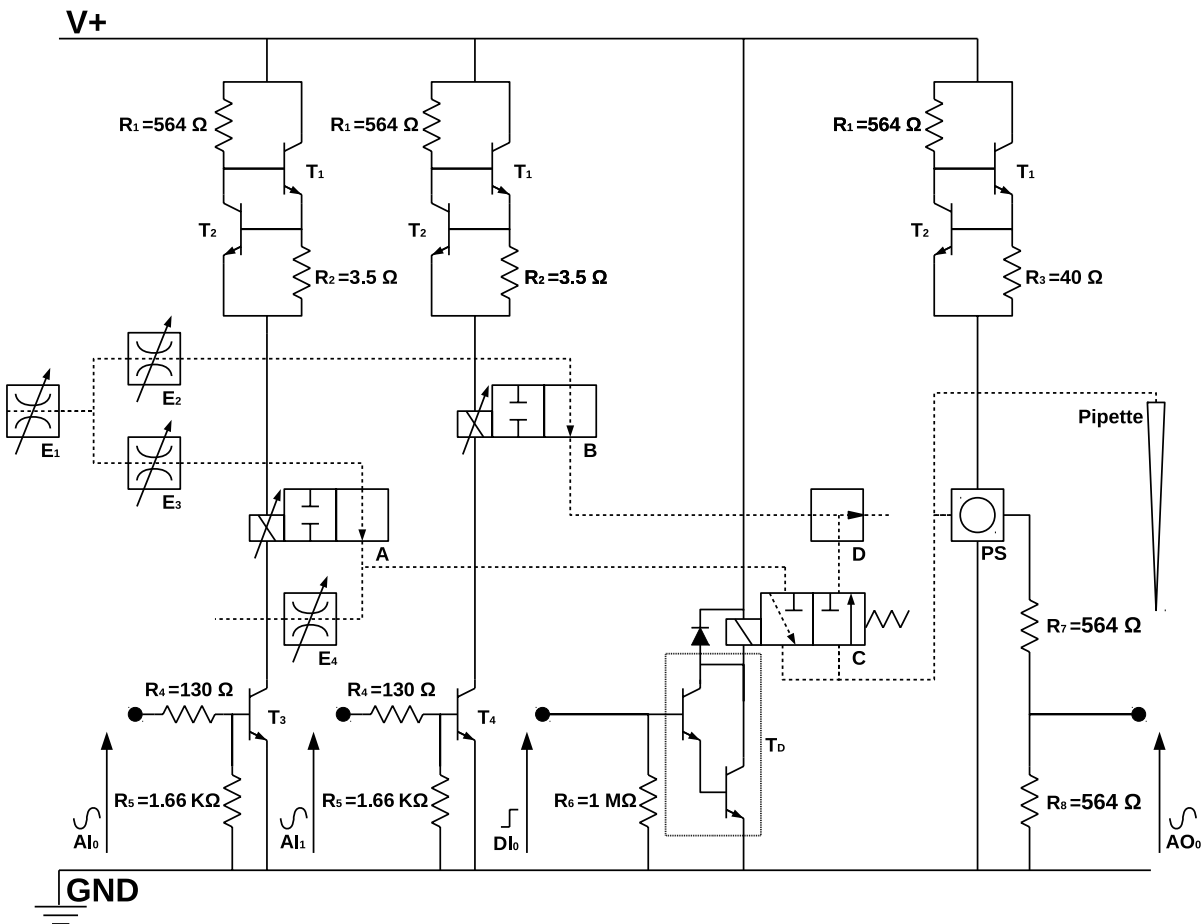


**Figure S5.** Related to Figure 1. Circuit schematics of the electro-pneumatic regulator. The electrical power supplied to A and B by the sub-circuits in the top left part of the schematics is regulated by two standard bipolar NPN power transistors ( $T_1$  and  $T_2$  - model BD 237, ST Microelectronics) controlled in the linear region ( $V_{be} = 0.5-1$  V). The top left electrical sub-circuits use the same type of BJT and implement two current limiters. The 3-port solenoid valve (C) is an on/off type device controlled through a NPN Darlington transistor ( $T_D$  - ZTX605, Digikey). A diode (IN916, Transys Electronics) is also included in the sub-circuit to protect this valve. The output port of C is then connected to the pipette and to a compound pressure sensor ([F] - PSE 543-M3, SMC Pneumatics) which provides the control system with the process variable values (1-5 V for -100 to +100 KPa). Terminal  $AO_0$  in the schematic is connected to the terminal  $AI_0$  of the microcontroller board. The proportional solenoidal valves A and B are controlled by means of two analogue signals generated by the 12-bit digital to analogue converter (DAC) on the microcontroller board. DAC output ranges from 0.58-2.8 V while the voltage range needed for the trans-conductance amplification is 0.5-1 V. Terminals  $AI_0$  and  $AI_1$  in the schematics are connected to the terminal  $AO_0$  and  $AO_1$  of the microcontroller. The control signals are in the range 0.5-1 V. Terminal  $DI_0$  in the schematics is connected to the terminal  $DO_0$  of the microcontroller.

## KEY RESOURCES TABLE

The table highlights the genetically modified organisms and strains, cell lines, reagents, software, and source data **essential** to reproduce results presented in the manuscript. Depending on the nature of the study, this may include standard laboratory materials (i.e., food chow for metabolism studies), but the Table is **not** meant to be comprehensive list of all materials and resources used (e.g., essential chemicals such as SDS, sucrose, or standard culture media don't need to be listed in the Table). **Items in the Table must also be reported in the Method Details section within the context of their use.** The number of **primers and RNA sequences** that may be listed in the Table is restricted to no more than ten each. If there are more than ten primers or RNA sequences to report, please provide this information as a supplementary document and reference this file (e.g., See Table S1 for XX) in the Key Resources Table.

**Please note that ALL references cited in the Key Resources Table must be included in the References list.** Please report the information as follows:

- **REAGENT or RESOURCE:** Provide full descriptive name of the item so that it can be identified and linked with its description in the manuscript (e.g., provide version number for software, host source for antibody, strain name). In the Experimental Models section, please include all models used in the paper and describe each line/strain as: model organism: name used for strain/line in paper: genotype. (i.e., Mouse: OXTR<sup>fl/fl</sup>; B6.129(SJL)-Oxtr<sup>tm1.1Wsy/J</sup>). In the Biological Samples section, please list all samples obtained from commercial sources or biological repositories. Please note that software mentioned in the Methods Details or Data and Software Availability section needs to be also included in the table. See the sample Table at the end of this document for examples of how to report reagents.
- **SOURCE:** Report the company, manufacturer, or individual that provided the item or where the item can be obtained (e.g., stock center or repository). For materials distributed by Addgene, please cite the article describing the plasmid and include "Addgene" as part of the identifier. If an item is from another lab, please include the name of the principal investigator and a citation if it has been previously published. If the material is being reported for the first time in the current paper, please indicate as "this paper." For software, please provide the company name if it is commercially available or cite the paper in which it has been initially described.
- **IDENTIFIER:** Include catalog numbers (entered in the column as "Cat#" followed by the number, e.g., Cat#3879S). Where available, please include unique entities such as [RRIDs](#), Model Organism Database numbers, accession numbers, and PDB or CAS IDs. For antibodies, if applicable and available, please also include the lot number or clone identity. For software or data resources, please include the URL where the resource can be downloaded. Please ensure accuracy of the identifiers, as they are essential for generation of hyperlinks to external sources when available. Please see the Elsevier [list of Data Repositories](#) with automated bidirectional linking for details. When listing more than one identifier for the same item, use semicolons to separate them (e.g. Cat#3879S; RRID: AB\_2255011). If an identifier is not available, please enter "N/A" in the column.
  - **A NOTE ABOUT RRIDs:** We highly recommend using RRIDs as the identifier (in particular for antibodies and organisms, but also for software tools and databases). For more details on how to obtain or generate an RRID for existing or newly generated resources, please [visit the RII](#) or [search for RRIDs](#).

Please use the empty table that follows to organize the information in the sections defined by the subheading, skipping sections not relevant to your study. Please do not add subheadings. To add a row, place the cursor at the end of the row above where you would like to add the row, just outside the right border of the table. Then press the ENTER key to add the row. You do not need to delete empty rows. Each entry must be on a separate row; do not list multiple items in a single table cell. Please see the sample table at the end of this document for examples of how reagents should be cited.

**TABLE FOR AUTHOR TO COMPLETE**

Please upload the completed table as a separate document. **Please do not add subheadings to the Key Resources Table.** If you wish to make an entry that does not fall into one of the subheadings below, please contact your handling editor. (NOTE: For authors publishing in Current Biology, please note that references within the KRT should be in numbered style, rather than Harvard.)

**KEY RESOURCES TABLE**

REAGENT or RESOURCE	SOURCE	IDENTIFIER
<b>Antibodies</b>		
<b>Bacterial and Virus Strains</b>		
<b>Biological Samples</b>		
<b>Chemicals, Peptides, and Recombinant Proteins</b>		
<b>Critical Commercial Assays</b>		
<b>Deposited Data</b>		
<b>Experimental Models: Cell Lines</b>		

Experimental Models: Organisms/Strains		
Mouse: C57BL/6	Harlan UK	
Mouse: GAD67-GFP	Margrie Laboratory	
Oligonucleotides		
Recombinant DNA		
Software and Algorithms		
Labview software	National Instrument	Labview 2012
Matlab software	MathWorks	Matlab 2013a
Sciscan software (ver 11 Dec 2014)	Scientifica Ltd	
Multiclamp commander software and relative dll file for third parties software interface	Axon Instruments	
Other		
Two photon microscope	Scientifica Ltd	
Galvanometric scanning mirrors	Cambridge Technology	6215H-671XX
Photo-multiplier tubes	Hamamatsu Photonics	R3896s
Dichroic beam splitter	Chroma Technology	T565LPXR
Optical filters	Chroma Technology	ET620/60M-2P
Optical filters	Chroma Technology	ET525/50M-2P
Mode-locked Ti-sapphire laser	Spectraphysics	Mai Tai HP
Water immersion objective, 0.8 N.A., 3.3 mm W.D.,	Olympus	LUMPLFLN-W 40x
Objective, plan achromat, 0.1 N.A., 18.5 mm W.D.	Olympus	RMS 4x
24 V / 65 W power supply	Maplin	N10NB
CCD Camera (based on a Sony CCD Progressive Scan Chip)	Scientifica Ltd	SciCam CCD Camera
Digital/analogue acquisition board	National Instruments	DAQ PCI-6110
Digital/analogue acquisition board	National Instruments	DAQ USB-6211
3axis micromanipulator	Scientifica Ltd	Multistar
Signal amplifier	Axon Instruments	Multiclamp 700B
Microcontroller (Arduino Due based on the Atmel SAM3X8E ARM Cortex-M3 CPU).	RS	Arduino Due



TABLE WITH EXAMPLES FOR AUTHOR REFERENCE

REAGENT or RESOURCE	SOURCE	IDENTIFIER
Antibodies		
Rabbit monoclonal anti-Snail	Cell Signaling Technology	Cat#3879S; RRID: AB_2255011
Mouse monoclonal anti-Tubulin (clone DM1A)	Sigma-Aldrich	Cat#T9026; RRID: AB_477593
Rabbit polyclonal anti-BMAL1	This paper	N/A
Bacterial and Virus Strains		
pAAV-hSyn-DIO-hM3D(Gq)-mCherry	Krashes et al., 2011	Addgene AAV5; 44361-AAV5
AAV5-EF1a-DIO-hChR2(H134R)-EYFP	Hope Center Viral Vectors Core	N/A
Cowpox virus Brighton Red	BEI Resources	NR-88
Zika-SMGC-1, GENBANK: KX266255	Isolated from patient (Wang et al., 2016)	N/A
<i>Staphylococcus aureus</i>	ATCC	ATCC 29213
<i>Streptococcus pyogenes</i> : M1 serotype strain: strain SF370; M1 GAS	ATCC	ATCC 700294
Biological Samples		
Healthy adult BA9 brain tissue	University of Maryland Brain & Tissue Bank; <a href="http://medschool.umaryland.edu/btbank/">http://medschool.umaryland.edu/btbank/</a>	Cat#UMB1455
Human hippocampal brain blocks	New York Brain Bank	<a href="http://nybb.hs.columbia.edu/">http://nybb.hs.columbia.edu/</a>
Patient-derived xenografts (PDX)	Children's Oncology Group Cell Culture and Xenograft Repository	<a href="http://cogcell.org/">http://cogcell.org/</a>
Chemicals, Peptides, and Recombinant Proteins		
MK-2206 AKT inhibitor	Selleck Chemicals	S1078; CAS: 1032350-13-2
SB-505124	Sigma-Aldrich	S4696; CAS: 694433-59-5 (free base)
Picrotoxin	Sigma-Aldrich	P1675; CAS: 124-87-8
Human TGF- $\beta$	R&D	240-B; GenPept: P01137
Activated S6K1	Millipore	Cat#14-486
GST-BMAL1	Novus	Cat#H00000406-P01

Critical Commercial Assays		
EasyTag EXPRESS 35S Protein Labeling Kit	Perkin-Elmer	NEG772014MC
CaspaseGlo 3/7	Promega	G8090
TruSeq ChIP Sample Prep Kit	Illumina	IP-202-1012
Deposited Data		
Raw and analyzed data	This paper	GEO: GSE63473
B-RAF RBD (apo) structure	This paper	PDB: 5J17
Human reference genome NCBI build 37, GRCh37	Genome Reference Consortium	<a href="http://www.ncbi.nlm.nih.gov/projects/genome/assembly/grc/human/">http://www.ncbi.nlm.nih.gov/projects/genome/assembly/grc/human/</a>
Nanog STILT inference	This paper; Mendeley Data	<a href="http://dx.doi.org/10.17632/wx6s4mj7s8.2">http://dx.doi.org/10.17632/wx6s4mj7s8.2</a>
Affinity-based mass spectrometry performed with 57 genes	This paper; and Mendeley Data	Table S8; <a href="http://dx.doi.org/10.17632/5hvpvspw82.1">http://dx.doi.org/10.17632/5hvpvspw82.1</a>
Experimental Models: Cell Lines		
Hamster: CHO cells	ATCC	CRL-11268
<i>D. melanogaster</i> : Cell line S2: S2-DRSC	Laboratory of Norbert Perrimon	FlyBase: FBtc0000181
Human: Passage 40 H9 ES cells	MSKCC stem cell core facility	N/A
Human: HUES 8 hESC line (NIH approval number NIHhESC-09-0021)	HSCI iPS Core	hES Cell Line: HUES-8
Experimental Models: Organisms/Strains		
<i>C. elegans</i> : Strain BC4011: srl-1(s2500) II; dpy-18(e364) III; unc-46(e177)rol-3(s1040) V.	Caenorhabditis Genetics Center	WB Strain: BC4011; WormBase: WBVar00241916
<i>D. melanogaster</i> : RNAi of Sxl: y[1] sc[*] v[1]; P{TRiP.HMS00609}attP2	Bloomington Drosophila Stock Center	BDSC:34393; FlyBase: FBtp0064874
<i>S. cerevisiae</i> : Strain background: W303	ATCC	ATCC: 208353
Mouse: R6/2: B6CBA-Tg(HDexon1)62Gpb/3J	The Jackson Laboratory	JAX: 006494
Mouse: OXTRfl/fl: B6.129(SJL)-Oxtr <sup>tm1.1Wsy/J</sup>	The Jackson Laboratory	RRID: IMSR_JAX:008471
Zebrafish: Tg(Shha:GFP)t10: t10Tg	Neumann and Nüsslein-Volhard, 2000	ZFIN: ZDB-GENO-060207-1
<i>Arabidopsis</i> : 35S::PIF4-YFP, BZR1-CFP	Wang et al., 2012	N/A
<i>Arabidopsis</i> : JYB1021.2: pS24(AT5G58010)::cS24:GFP(-G):NOS #1	NASC	NASC ID: N70450
Oligonucleotides		
siRNA targeting sequence: PIP5K I alpha #1: ACACAGUACUCAGUUGAUA	This paper	N/A
Primers for XX, see Table SX	This paper	N/A
Primer: GFP/YFP/CFP Forward: GCACGACTTCTTCAAGTCCGCCATGCC	This paper	N/A
Morpholino: MO-pax2a GGTCTGCTTTGCAGTGAATATCCAT	Gene Tools	ZFIN: ZDB-MRPHLNO-061106-5

ACTB (hs01060665_g1)	Life Technologies	Cat#4331182
RNA sequence: hnRNPA1_ligand: UAGGGACUUAGGGUUCUCUCUAGGGACUUAG GGUUCUCUCUAGGGA	This paper	N/A
<b>Recombinant DNA</b>		
pLVX-Tight-Puro (TetOn)	Clontech	Cat#632162
Plasmid: GFP-Nito	This paper	N/A
cDNA GH111110	Drosophila Genomics Resource Center	DGRC:5666; FlyBase:FBcl013041 5
AAV2/1-hsyn-GCaMP6- WPRE	Chen et al., 2013	N/A
Mouse raptor: pLKO mouse shRNA 1 raptor	Thoreen et al., 2009	Addgene Plasmid #21339
<b>Software and Algorithms</b>		
Bowtie2	Langmead and Salzberg, 2012	<a href="http://bowtie-bio.sourceforge.net/bowtie2/index.shtml">http://bowtie- bio.sourceforge.net/ bowtie2/index.shtml</a>
Samtools	Li et al., 2009	<a href="http://samtools.sourceforge.net/">http://samtools.sourc eforge.net/</a>
Weighted Maximal Information Component Analysis v0.9	Rau et al., 2013	<a href="https://github.com/ChristophRau/wMICA">https://github.com/C hristophRau/wMICA</a>
ICS algorithm	This paper; Mendeley Data	<a href="http://dx.doi.org/10.17632/5hvpvpspw82.1">http://dx.doi.org/10.1 7632/5hvpvpspw82.1</a>
<b>Other</b>		
Sequence data, analyses, and resources related to the ultra-deep sequencing of the AML31 tumor, relapse, and matched normal.	This paper	<a href="http://aml31.genome.wustl.edu">http://aml31.genome .wustl.edu</a>
Resource website for the AML31 publication	This paper	<a href="https://github.com/chrisamiller/aml31SuppSite">https://github.com/ch risamiller/aml31Supp Site</a>



Click here to access/download  
**ZIP File**  
uploading.zip

